Earth and Space Science

Key Points:

- The modulation of Es layers by gravity waves (GWs) (1,350 km > λ_h > 156 km) is simulated
- GWs cause short-period (1.2–3 hr) Fe^+ density perturbations, leading to production of fine structure in mid-latitude Es layers
- Longitudinal dependence in Fe^+ density perturbations is mainly explained by the longitudinal distribution of GWs activity in the mesosphere and lower thermosphere region

Numerical Simulations of Metallic Ion Density Perturbations in Sporadic E Layers Caused by Gravity Waves

Lihui Qiu[1,2] ![ORCID], Yosuke Yamazaki[2] ![ORCID], Tao Yu[1] ![ORCID], Erich Becker[3] ![ORCID], Yasunobu Miyoshi[4], Yifan Qi[1], Tarique A. Siddiqui[2] ![ORCID], Claudia Stolle[2] ![ORCID], Wuhu Feng[5,6] ![ORCID], John M. C. Plane[6] ![ORCID], Yu Liang[1], and Huixin Liu[4] ![ORCID]

[1]Institute of Geophysics & Geomatics, China University of Geosciences, Wuhan, China, [2]Leibniz Institute of Atmospheric Physics at the University of Rostock, Kühlungsborn, Germany, [3]Northwest Research Associates Inc., Boulder, CO, USA, [4]Department of Earth and Planetary Sciences, Kyushu University, Fukuoka, Japan, [5]National Centre for Atmospheric Science, University of Leeds, Leeds, UK, [6]School of Chemistry, University of Leeds, Leeds, UK

Abstract Tidal signatures in sporadic E (Es) layer have been confirmed by observations and simulations. However, the effect of gravity waves (GWs) on the Es layer formation process has not yet been fully understood. In this paper, the modulation of Es layers by GWs is examined through numerical simulations, in which a physics-based model of Es layer is forced by neutral winds from the High Altitude Mechanistic General Circulation Model that can resolve GWs with horizontal wavelengths longer than 156 km (λ_h > 156 km). Comparison of the simulation results with and without the GWs (1,350 km > λ_h > 156 km) forcing reveals that the inclusion of GWs leads to short-period (1.2–3 hr) density perturbations in Es layers, which are also seen in ground-based ionosonde observations. At a given time, the metallic ion density at altitudes between 120 and 150 km can either increase (by up to ∼+600%) or reduce (by up to −90%) in response to GW forcing. The relative density perturbations are smaller (by up to 60%) between 90 and 120 km altitude. It is also found that the GW effect on the metallic ion density relates to the longitude, which is mostly explained by the geographical distribution of GWs activity in the mesosphere and lower thermosphere region. The longitudinal variation of the background geomagnetic field plays only a secondary role.

1. Introduction

Ionospheric sporadic E (Es) layers are thin layers of concentrated metallic ions (mainly Fe^+, Mg^+, Si^+, Na^+, and Ca^+) that intermittently appear in the mesosphere and lower thermosphere (MLT) region (Whitehead, 1989). Es layers usually have a thickness of 1–5 km (Qiu et al., 2021; Tsai et al., 2018; Zeng & Sokolovskiy, 2010) with a horizontal extent of 50–3,000 km (Maeda & Heki, 2014, 2015; Sun et al., 2021). Es layers can cause reflection, scattering and fading of radio signals, leading to a transient loss of signal in communication and navigation (Deacon et al., 2020; Yue et al., 2016).

The classic and widely accepted midlatitude Es layer formation mechanism is the wind shear theory (Whitehead, 1960). This has been confirmed by observations (e.g., Bishop et al., 2005; Yamazaki et al., 2021) and simulations (e.g., Andoh et al., 2022; Qiu et al., 2019; Shinagawa et al., 2017; B. Yu et al., 2019). Observations from Rockets and satellites show that large wind shear exists around 105 km in the MLT region (e.g., Larsen, 2002; Yamazaki et al., 2023). And, the geographical distribution and seasonal variation of mid-latitude Es layers can be largely attributed to the geographical and seasonal dependence of vertical wind shear (Qiu et al., 2023; Shinagawa et al., 2017; Yamazaki et al., 2021). The layer-forming process is also affected by atmospheric tides forced by solar radiation (Haldoupis, 2011). The diurnal, semidiurnal (Arras et al., 2009; Haldoupis, 2004), terdiurnal, and quarterdiurnal (Fytterer et al., 2014; Jacobi et al., 2019; Sobhkhiz-Miandehi et al., 2022) tidal components of the Es layer occurrence rate have been revealed by observations.

The tidal behavior of Es layers has been satisfactorily modeled (Andoh et al., 2022; Resende et al., 2016). However, Es layer variability caused by atmospheric gravity waves (GWs) has not yet been fully understood. GWs with periods shorter than atmospheric tides play a significant role in transporting energy and momentum to the MLT region (Fritts & Alexander, 2003; Lu et al., 2009), contributing to the production of strong winds and wind shears (X. Liu et al., 2014). GWs can affect the distribution of minor species (e.g., atomic oxygen) and electron density in the MLT region (Hickey & Walterscheid, 2001; Hocke & Tsuda, 2001; Wang et al., 2021), and even propagate into the ionospheric F region to cause electron density disturbances (Hickey et al., 2009; H. Liu et al., 2017).

Investigation: Lihui Qiu
Methodology: Lihui Qiu, Yifan Qi, Yu Liang
Resources: Yosuke Yamazaki, Erich Becker, Yasunobu Miyoshi, Tarique A. Siddiqui, Claudia Stolle, Wuhu Feng, John M. C. Plane
Supervision: Yosuke Yamazaki, Tao Yu
Validation: Yosuke Yamazaki
Visualization: Lihui Qiu
Writing – original draft: Lihui Qiu
Writing – review & editing: Yosuke Yamazaki, Erich Becker, Yasunobu Miyoshi, Tarique A. Siddiqui, Claudia Stolle, Wuhu Feng, John M. C. Plane, Huixin Liu

Huang and Kelley (1996) used a computer simulation to study GW modulation of existing Es layers and demonstrated that a horizontally stratified Es layer can be deformed by GWs and become a quasi-periodic wavelike structure. Using the non-dissipative linear GW model, Didebulidze et al. (2020) simulated the formation of multi-layered Es and suggested theoretically that GWs can cause heavy metallic ion redistribution.

In the present study we use a 1-D Es layer model (Zuo et al., 2006) driven by neutral winds from the Ground-to-topside model of Atmosphere and Ionosphere for Aeronomy model (GAIA; Miyoshi & Fujiwara, 2003; Kobayashi et al., 2015), Whole Atmosphere Community Climate Model with thermosphere and ionosphere eXtension model (WACCM-X 2.1; H.-L. Liu et al., 2018), and High Altitude Mechanistic general Circulation Model (HIAMCM; Becker & Vadas, 2020; Becker et al., 2022) to examine the physical process of Es layer evolution, respectively. First, we compare the HIAMCM's capability to reproduce the tidal variation in Es layers with GAIA and WACCM-X that were used in previous studies (e.g., Andoh et al., 2022; Wu et al., 2021). Second, we focus on the physical process of Es layer evolution modulated by GWs, which is not taken into account in previous work.

2. Models and Observations

This work used an Es layer model (Zuo et al., 2006) and six ionosondes located at middle latitudes to simulate and observe the Es layer evolution process during the summer of 10–11 July 2007. The Es model solves for the altitude profile of the Fe^+ density as a function of time, based on the ion continuity and velocity equations. The ion continuity equation is given by

$$\frac{\partial N_i}{\partial t} + \frac{\partial (N_i V_{iz})}{\partial z} = q_i - L_i N_i \qquad (1)$$

where N_i is the number density of Fe^+, z is altitude, and q_i and L_i represent the chemical production and loss rates, respectively. Our simulations focus on the dynamical processes of Fe^+, assuming chemical steady state ($q_i - L_i N_i = 0$) (Didebulidze et al., 2020). The vertical velocity of Fe^+, V_{iz} is given by

$$V_{iz} = \frac{dz}{dt} = \frac{1}{\gamma^2 + 1} \left[U_x \sin\theta \cos\theta + \gamma U_y \cos\theta + U_z (\gamma^2 + \sin\theta^2) \right] \qquad (2)$$

where γ is the ratio of the ion-neutral collision frequency (ν_i) to the ion gyrofrequency (ω_i) (Nygren et al., 1984). U_x, U_y, and U_z are the southward, eastward and upward winds, respectively. The geomagnetic inclination θ is obtained from the International Geomagnetic Reference Field (IGRF11) (Finlay et al., 2010). The neutral winds are derived from atmospheric models, which will be described later. The initial density profile of Fe^+ is derived from the WACCM-Fe model, which is a global atmospheric model of meteoric iron (Feng et al., 2013). The ion continuity Equation 1 is solved by the finite difference method with a time step of 5 s and an altitude resolution of 500 m. The altitude range is from 80 to 150 km. The boundary conditions are set as $\partial N_i/\partial t = 0$.

Three atmospheric models are used to provide neutral wind inputs to the Es layer model: namely, HIAMCM (Becker & Vadas, 2020; Becker et al., 2022), GAIA (Kobayashi et al., 2015; Miyoshi & Fujiwara, 2003), and WACCM-X 2.1 (H.-L. Liu et al., 2018). HIAMCM is a high-resolution whole atmosphere model that extends from the surface to ~450 km altitude. The model is nudged by the Modern-Era Retrospective analysis for Research and Applications version 2 (MERRA-2; Gelaro et al., 2017) reanalysis data up to the altitude of ~70 km. It can output the winds that contains *total waves* (horizontal wavelengths $\lambda_h > 156$ km) and *large-scale waves* ($\lambda_h > 1,350$ km) (Becker & Vadas, 2020; Becker et al., 2022).

The GAIA model is an upper extension of the Kyushu University General Circulation Model (Miyahara et al., 1993) that extends to the exobase at an altitude of ~500 km. The neutral atmosphere part of GAIA assimilates meteorological reanalysis data below 30 km (Japanese 55-year Reanalysis; Kobayashi et al., 2015) by a nudging method (Jin et al., 2008). It has a grid of 2.8° longitude by 2.8° latitude horizontally. The GAIA model can simulate the large-scale waves with $\lambda_h > 1,000$ km. The effect of GWs with $\lambda_h < 1,000$ km on the background winds is taken into account by GW-drag parameterization (Miyoshi & Fujiwara, 2003; Sato & Yasui, 2018).

The WACCM-X 2.1 is a whole atmosphere model developed by the National Center for Atmospheric Research. It can self-consistently resolves the dynamic and physical processes from the surface to ~700 km altitude (H.-L. Liu et al., 2018), which is also constrained by the MERRA-2 reanalysis data. The horizontal resolution is 1.9° in
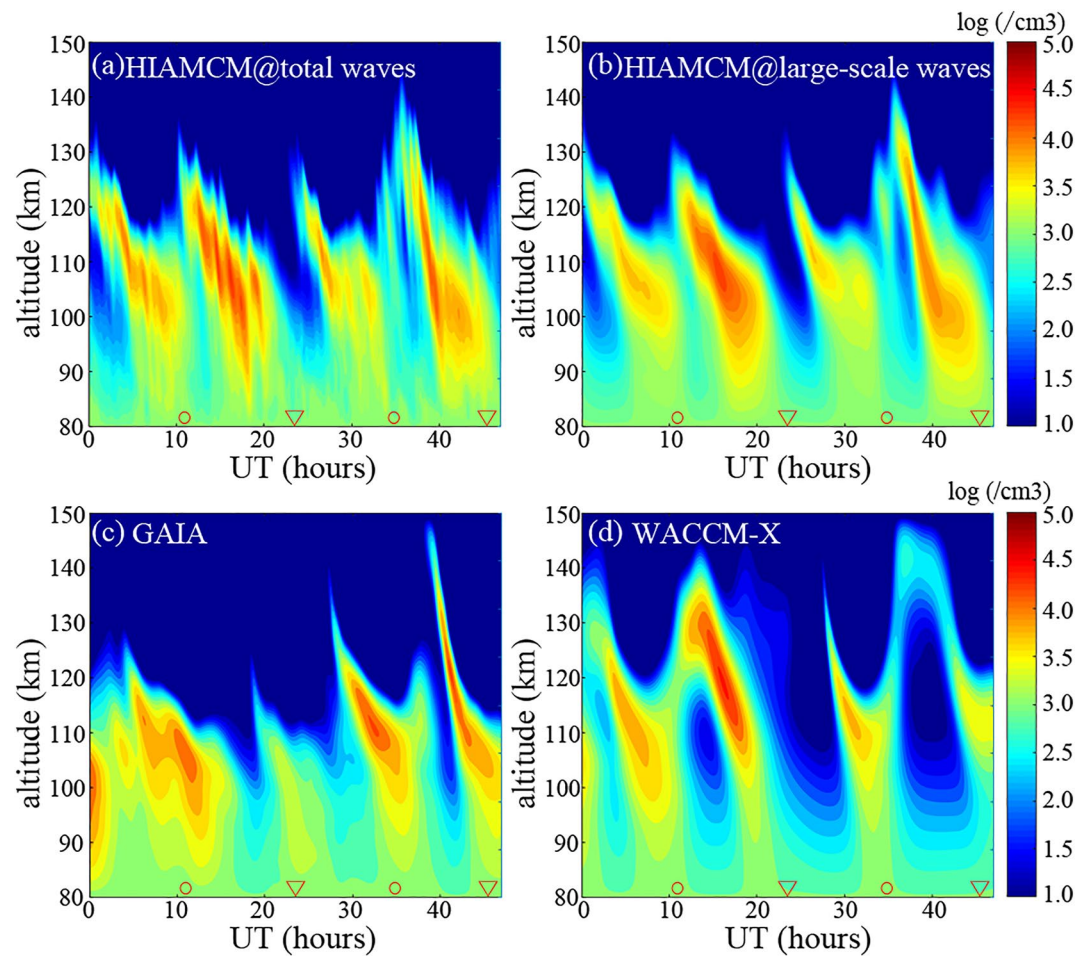
Figure 1. Examples of the temporal variations of simulated Fe$^+$ density at San Vito (18°E, 40°N) derived from Es layer model driven by neutral winds from (a) High Altitude Mechanistic General Circulation Model (HIAMCM) with *total waves* (horizontal wavelength larger than ~156 km), (b) HIAMCM with only *large-scale waves* (horizontal wavelength larger than ~1,350 km), (c) GAIA, and (d) WACCM-X. The simulations were run for 72 hr and the first 24 hr were discarded. ○ and ▽ on the horizontal axis represent the local noon (12:00 LT) and local midnight (24:00 LT), respectively.

latitude and 2.5° in longitude. As in the case of GAIA, the effect of GWs on the background winds is taken into account by GW-drag parameterization, but GWs with $\lambda_h < 1,000$ km are not resolved.

The six ionosondes used in this study are located at Rome (USRI-Code: RO041, 12°E, 42°N), San Vito (USRI-Code: VT139, 18°E, 40°N), Athens (USRI-Code: AT138, 24°E, 38°N), An Yang (USRI-Code: AN438, 127°E, 37°N), Pt Arguello (USRI-Code: PA836, 240°E, 35°N), and El Arenosillo (USRI-Code: EA036, 354°E, 37°N). The foEs (critical sporadic E frequency) is used to quantify the Es layer variability. The time resolution is 30 min at An Yang and El Arenosillo stations and 15 min at other stations.

3. Results

Figure 1 compares the simulated Fe$^+$ densities derived from the Es layer model driven by HIAMCM with *total waves*, HIAMCM with only *large-scale waves*, GAIA, and WACCM-X in panels (a–d), to confirm the HIAM-CM's capability to reproduce the tidal variation in Es layers and highlight what was not taken into account in previous work. The semidiurnal variation in Fe$^+$ density is reproduced through the Es layer model driven by HIAMCM, which is consistent with previous results (e.g., Andoh et al., 2022), suggesting that the Es layer (Fe$^+$ density $>$~3.5×10^3 cm^{-3}) occurrences are mainly controlled by neutral wind shears associated with atmospheric tides (Figure S1 in Supporting Information S1). Compared with the simulations in Figures 1b–1d, Figure 1a shows some fine structures of Es layers, which is not simulated in previous results (e.g., Andoh et al., 2022; Wu
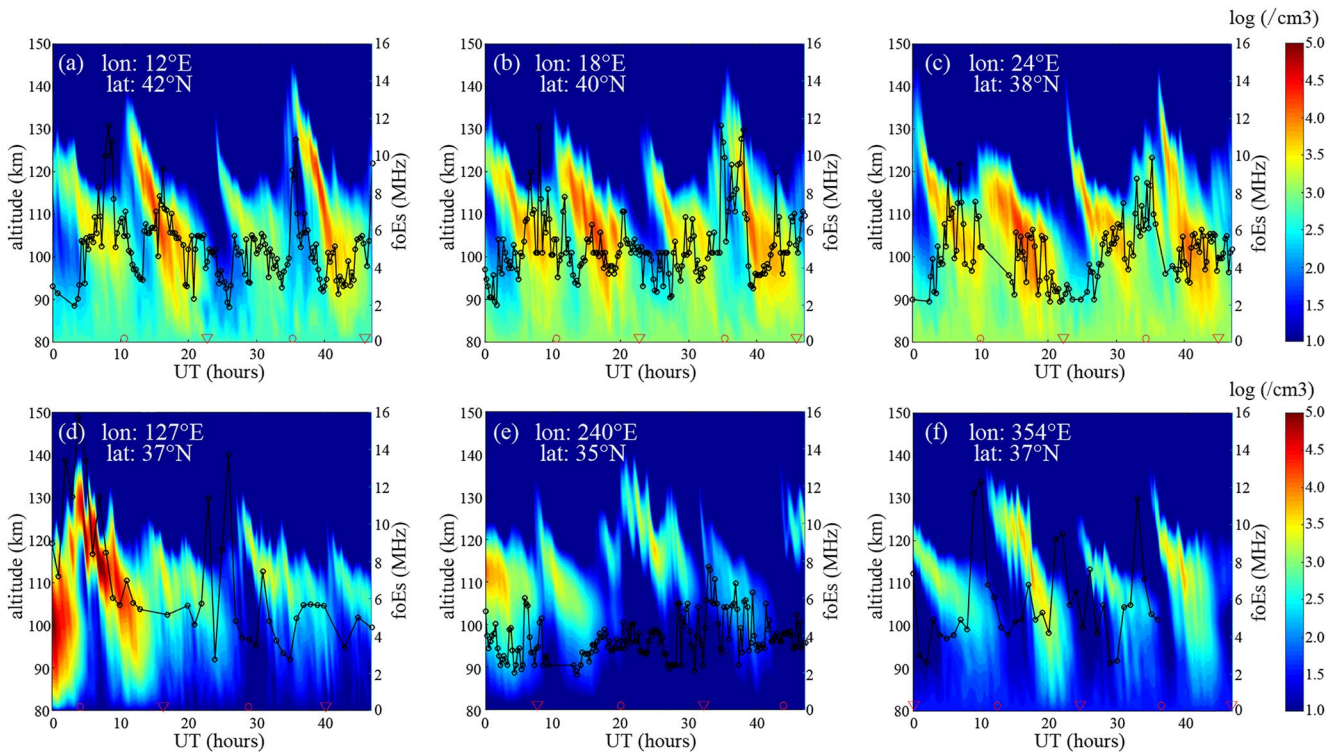
Figure 2. The temporal variations of simulated Fe$^+$ density and observed foEs (Es critical frequency) over six mid-latitude stations during 10–11 July 2007. The Es layer model is driven by neutral winds from High Altitude Mechanistic General Circulation Model with *total waves* (horizontal wavelength larger than ~156 km). The black solid lines represent the foEs recorded by ionosondes. The simulations were run for 72 hr and the first 24 hr were discarded. ∘ and ▽ on the horizontal axis represent the local noon (12:00 LT) and local midnight (24:00 LT), respectively.

et al., 2021). This is because HIAMCM can simulate GWs down to horizontal wavelengths of 156 km (Becker & Vadas, 2020), which drive the short-period perturbations in Fe$^+$ density within the Es layers. Note that the difference between Figures 1b–1d may be caused by differences in parameterizations of the physical processes, such as GW drag parameterization and solar radiation parameterization, and meteorological reanalysis data used in the atmospheric models.

Figure 2 shows the temporal variations of simulated Fe$^+$ density and observed foEs over six mid-latitude stations during 10–11 July 2007. The Es layer model is driven by neutral winds from HIAMCM with *total waves*. The black solid lines represent the foEs recorded by ionosondes. First, both simulations and observations show that the Es layers tend to exhibit semidiurnal variations. Second, the longitudinal variations of simulated Fe$^+$ density also agree reasonably well with the observations. Third, short-period perturbations (1.2–3 hr) in the Es layers are displayed in both simulations and observations.

Figure 3 shows the relative Fe$^+$ density perturbation (ΔFe$^+$) due to GWs (1,350 km > λ_h > 156 km), over the six mid-latitude stations during 10–11 July 2007. The ΔFe$^+$ is given by (Fe$^+_{\text{total waves}}$ − Fe$^+_{\text{large−scale waves}}$)/(Fe$^+_{\text{large−scale waves}}$) where the Fe$^+_{\text{total waves}}$ is the simulated Fe$^+$ density with *total waves*, and Fe$^+_{\text{large−scale waves}}$ is the simulated Fe$^+$ density with only the *large-scale waves*. On the one hand, GWs modulate the Fe$^+$ density more effectively at higher altitudes (above 120 km) than at lower altitudes. The Fe$^+$ density can be increased by 200%–600% or completely dispersed above 120 km, but changes by only about 60% below 120 km. On the other hand, Fe$^+$ density perturbations also show clear longitudinal dependence, being stronger over An Yang (127°E, 37°N) than other stations.

4. Discussion

The simulation experiments in this study suggest that GWs can modulate the intensity and structure of Es layers. The Fe$^+$ density shows short-period perturbations (1.2 hr at ~135 km altitude, 3 hr at ~100 km altitude) (Figure S2 in Supporting Information S1), when GWs (1,350 km > λ_h > 156 km) are included in the simulation. This means
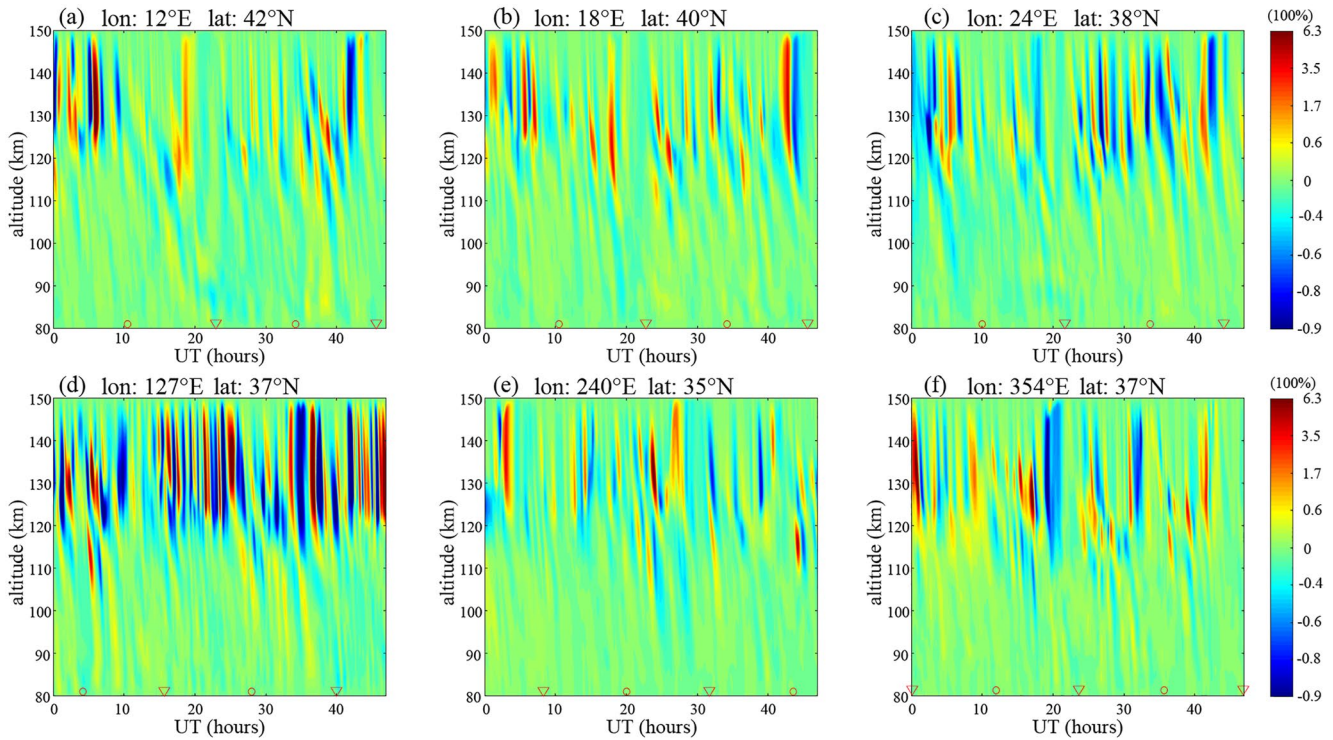
Figure 3. The Fe$^+$ density perturbations caused by gravity waves (horizontal wavelength larger than 156 km and smaller than 1,350 km) over six mid-latitude stations during 10–11 July 2007. ∘ and ▽ on the horizontal axis represent the local noon (12:00 LT) and local midnight (24:00 LT), respectively.

that upward-propagating GWs can cause sharp density gradient within Es layers. Miyoshi and Fujiwara (2008) examined the characteristics of GWs in the MLT region and found that the dominant periods of GWs for zonal wave number 80 ($\lambda_h \approx 500$ km) is 1.5–2 hr at 100 km altitude, which is basically consistent with the period of the Fe$^+$ density perturbations in our simulation results. The observations of foEs (Figure 2) also show perturbations at this period range.

The altitude dependences can be seen in the amplitude of ΔFe$^+$. The ΔFe$^+$ is largest at 120–150 km (Figure 3). At lower altitudes (below 120 km), the GWs can still increase or reduce the Fe$^+$ density by about 60%. The modulation of GWs on metallic ion density is more effective at higher altitudes where the geomagnetically-driven vertical plasma transport is less hindered by ion-neutral collisions (Haldoupis, 2018). It is also worth mentioning that ion-molecule chemistry reactions (Plane et al., 2015) and ion ambipolar diffusion (Didebulidze et al., 2020) may affect the modulation of GWs on the Es layer intensity, which should be further examined through simulation and observation in the future. Besides, the Fe$^+$ perturbations moving downward with time, indicating an upward energy propagation of GWs. Above 120 km their phase velocity (or vertical wavelength) is very large, so they appear to have "quasi-vertical" structure.

Figure 3 also shows that the amplitude of the GW-induced ΔFe$^+$ relates to the longitude. This is further highlighted in Figure 4a using the vertical ion convergence (VIC = $-\partial V_{iz}/\partial z$, where V_{iz} is the vertical velocity of Fe$^+$). It is known that VIC is that main physical parameter which controls the metallic ion density (Shinagawa et al., 2017). VIC is affected by both the wind shear caused by GWs and the geomagnetic field. Figure 4a shows the longitudinal distribution of the VIC perturbations due to GWs forcing (1,350 km > λ_h > 156 km) at an altitude of 120 km and a latitude of 36°N. The variance of the VIC perturbations evaluated at each longitude is displayed in Figure 4b (blue line). The VIC variance shows a double-peak longitudinal structure. One local maximum is in the East Asian region (∼100°E) and another local maximum is in the American region (∼300°E).

The longitudinal dependence of the VIC variance can result from (a) the longitudinal variation of GWs activity and (b) the longitudinal variation of the geomagnetic field. In what follows, the relative importance of the two is examined. Figure 4c shows the global distribution of the kinetic energy of GWs (E_k) at 120 km altitude during 10–11 July 2007, which is given by $E_k = 1/2\left[\overline{u'^2} + \overline{v'^2} + \overline{w'^2}\right]$ (Tsuda et al., 2000), where u', v', and w' are the
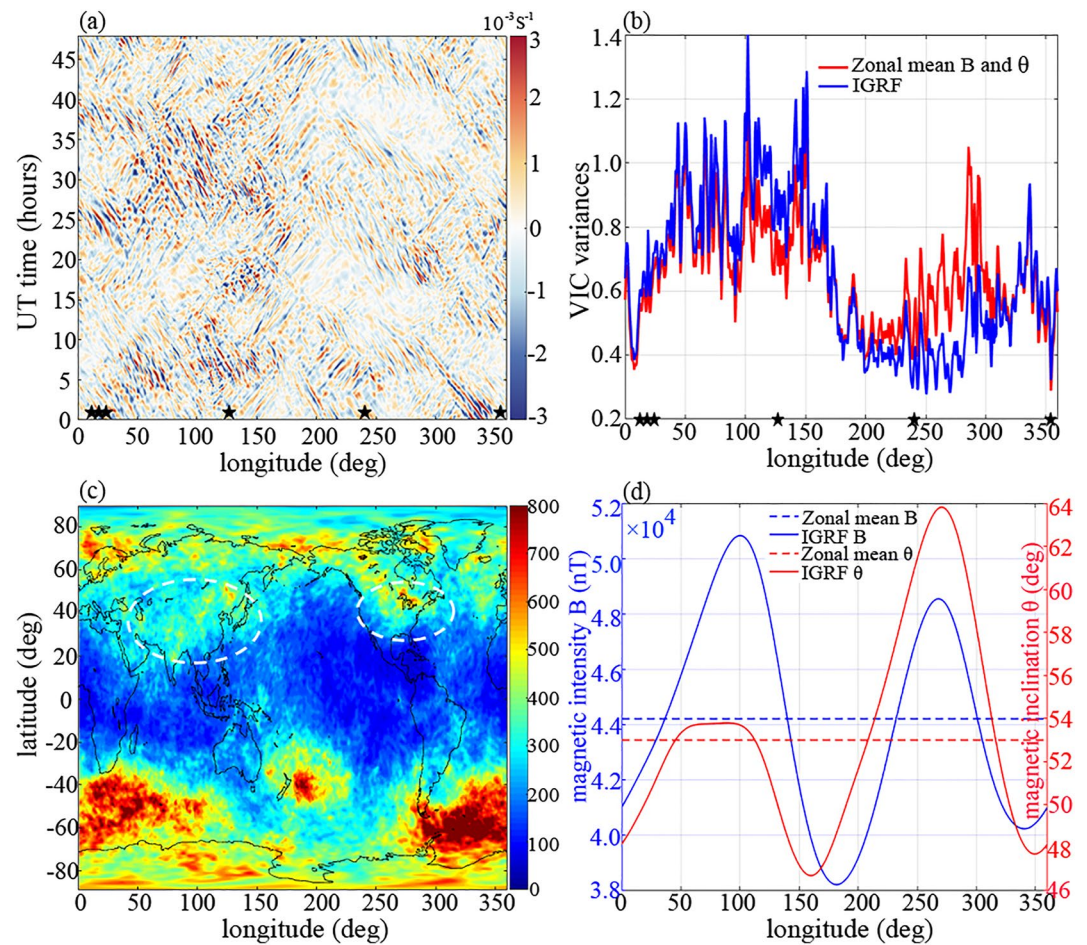
Figure 4. (a) Longitudinal variability of vertical ion convergence (VIC $= -\partial V_{iz}/\partial z$) at an altitude of 120 km and a latitude of 36°N. The black star symbols represent the locations of the five ionosondes. (b) Longitudinal variability of VIC variances. The blue line represents the results where the geomagnetic field is derived from IGRF11 (blue and red solid lines in panel (d)). The red line represents the results when the geomagnetic field is assumed to be longitudinally invariant (blue and red dashed lines in panel (d)). (c) Global distribution of the kinetic energy of gravity waves at 120 km altitude. (d) Longitudinal variability of magnetic intensity B (blue solid line) and inclination θ (red solid line) at an altitude of 120 km and a latitude of 36°N. The zonal mean magnetic intensity B (blue dashed line) and inclination θ (red dashed line).

zonal, meridional, and vertical wind perturbations caused by GWs (1,350 km $> \lambda_h >$ 156 km). At mid-latitudes in the northern hemisphere, there are two GWs energy enhancements over East Asia and America, which corresponds to the two peak regions of the VIC variance. Miyoshi et al. (2014) investigated the global view of GWs activity ($\lambda_h >$ 380 km) in the lower thermosphere. At mid-latitudes in the northern hemisphere, there are two regions with enhanced GWs activity near ~100°E and ~300°E, which agrees with our results (Figure 4c).

The geomagnetic field configuration also affects the VIC (Haldoupis, 2011; Whitehead, 1960). In Figure 4b, the red line represents VIC variances as the blue line but the intensity B and inclination θ of the geomagnetic field are replaced with their corresponding zonal mean values (blue and red dashed lines in Figure 4d) so that the geomagnetic field is longitudinally invariant. The difference between the blue and red lines represents the effect of the inhomogeneous geomagnetic field. The difference is relatively small, suggesting that the longitudinal dependence of the VIC variance is primarily caused by the longitudinal variation of GWs activity rather than the longitudinal variation of the geomagnetic field. Nevertheless, the effect of the geomagnetic field on the VIC variance is visible, especially in the East Asian (~120°E) and American (~270°E) sectors. According to the zonal wind shear mechanism, $(U_y \nu_{in} Be/m_i) \cos \theta \times (m_i^2)/(m_i^2 \nu_{in}^2 + B^2 e^2)$, the stronger magnetic intensity B and lower magnetic inclination θ favor the formation of Es layer, where m_i is the ion mass, e is the ion charge, and ν_{in} is ion-neutral collision frequency. Figure 4d shows the longitudinal variations of B (blue solid line) and θ (red

solid line) at a latitude of 36°N. In the East Asian sector, the strong magnetic field and low magnetic inclination contribute to an increase of the VIC variance, while in the American sector, the large magnetic inclination suppresses the VIC variance.

The Es layer model in this paper successfully simulates the short-period variations within Es layers. However, the model does not simulate all the observed foEs peaks (Figure 2), firstly because variability of the electric field, turbulence, and sudden injection of meteoric ions all affect Es layer formation; and secondly, because our 1-D model does not capture the horizontal advection of metallic ions and inhomogeneity of the horizontal wind.

5. Conclusions

This work examined the physical process of Es layer evolution at middle latitudes during the summer of the 10–11 July 2007 by using an Es layer model driven by neutral winds from the HIAMCM model that includes the GWs ($\lambda_h > 156$ km). The simulation results reproduce the tidal variations in Es layers, which agrees with the previous results from the Es layer model driven by GAIA and WACCM-X models. Besides, the inclusion of GWs in the simulations reveals fine structure in the Es layers caused by short-period (1.2–3 hr) GW-driven perturbations of the metallic ion density. The ion density can be increased by 200%–600% or completely dispersed between 120 and 150 km altitudes. The amplitude of ion density perturbations is about 60% between 90 and 120 km altitudes. In addition, metallic ion density perturbations also show longitudinal dependence, being stronger over East Asia (∼50–150°E), which is mainly explained by the geographical distribution of GW activity in the MLT region.

Data Availability Statement

The ionosonde data for this paper are available at: https://giro.uml.edu/didbase/scaled.php. The GAIA data are available at: https://gaia-web.nict.go.jp/data_e.html. The WACCM-X model source code can be found here (https://www2.hao.ucar.edu/modeling/waccm-x). The HIAMCM model simulations were performed by Erich Becker. Model documentations can be found in Becker and Vadas (2020) and Becker et al. (2022). The data used in the present simulations can been found in T. Yu (2023).

References

Andoh, S., Saito, A., & Shinagawa, H. (2022). Numerical simulations on day-to-day variations of low-latitude Es layers at Arecibo. *Geophysical Research Letters*, *49*(7), e2021GL097473. https://doi.org/10.1029/2021GL097473

Arras, C., Jacobi, C., & Wickert, J. (2009). Semidiurnal tidal signature in sporadic E occurrence rates derived from GPS radio occultation measurements at higher midlatitudes. *Annales Geophysicae*, *27*(6), 2555–2563. https://doi.org/10.5194/angeo-27-2555-2009

Becker, E., & Vadas, S. L. (2020). Explicit global simulation of gravity waves in the thermosphere. *Journal of Geophysical Research: Space Physics*, *125*(10), e2020JA028034. https://doi.org/10.1029/2020JA028034

Becker, E., Vadas, S. L., Bossert, K., Harvey, V. L., Zülicke, C., & Hoffmann, L. (2022). A high-resolution whole-atmosphere Model with resolved gravity and specified large-scale dynamics in the troposphere and stratosphere. *Journal of Geophysical Research: Atmospheres*, *127*(2), e2021JD035018. https://doi.org/10.1029/2021JD035018

Bishop, R. L., Earle, G. D., Larsen, M. F., Swenson, C. M., Carlson, C. G., Roddy, P. A., et al. (2005). Sequential observations of the local neutral wind field structure associated with E region plasma layers. *Journal of Geophysical Research*, *110*(A4), A04309. https://doi.org/10.1029/2004JA010686

Deacon, C. J., Witvliet, B. A., Steendam, S. N., & Mitchell, C. N. (2020). Rapid and accurate measurement of polarization and fading of weak VHF signals obliquely reflected from sporadic-E layers. *IEEE Transactions on Antennas and Propagation*, *69*(7), 4033–4048. https://doi.org/10.1109/TAP.2020.3044654

Didebulidze, G., Dalakishvili, G., & Todua, M. (2020). Formation of multilayered sporadic E under an influence of atmospheric gravity waves (AGWs). *Atmosphere*, *11*(6), 653. https://doi.org/10.3390/atmos11060653

Feng, W. H., Marsh, D. R., Chipperfield, M. P., Janches, D., Höffner, J., Yi, F., & Plane, M. C. J. (2013). A global atmospheric model of meteoric iron. *Journal of Geophysical Research: Atmospheres*, *118*(16), 9456–9474. https://doi.org/10.1002/jgrd.50708

Finlay, C. C., Maus, S., Beggan, C. D., Bondar, T. N., Chambodut, A., Chernova, T. A., et al. (2010). International geomagnetic reference field: The eleventh generation. *Geophysical Journal International*, *183*(3), 1216–1230. https://doi.org/10.1111/j.1365-246X.2010.04804.x

Fritts, D. C., & Alexander, M. J. (2003). Gravity wave dynamics and effects in the middle atmosphere. *Reviews of Geophysics*, *41*(1), 1003. https://doi.org/10.1029/2001RG000106

Fytterer, T., Arras, C., Hoffmann, P., & Jacobi, C. (2014). Global distribution of the migrating terdiurnal tide seen in sporadic E occurrence frequencies obtained from GPS radio occultations. *Earth Planets and Space*, *66*(1), 79. https://doi.org/10.1186/1880-5981-66-79

Gelaro, R., McCarty, W., Suárez, M. J., Todling, R., Molod, A., Takacs, L., et al. (2017). The Modern-Era Retrospective Analysis for Research and Applications, Version 2 (MERRA-2). *Journal of Climate*, *30*(14), 5419–5454. https://doi.org/10.1175/JCLI-D-16-0758.1

Haldoupis, C. (2011). A tutorial review on sporadic E layers. *Aeronomy of the Earth's Atmosphere and Ionosphere* (pp. 381–394). https://doi.org/10.1007/978-94-004-0326-1_29

Haldoupis, C. (2018). Is there a conclusive evidence on lightning-related effects on sporadic E layers? *Journal of Atmospheric and Solar-Terrestrial Physics*, *172*, 117–121. https://doi.org/10.1016/j.jastp.2018.03.024

Haldoupis, C., Pancheva, D., & Mitchell, N. J. (2004). A study of tidal and planetary wave periodicities present in midlatitude sporadic E layers. *Journal of Geophysical Research*, *109*(A2), A02302. https://doi.org/10.1029/2003JA010253

Hickey, M. P., Schubert, G., & Walterscheid, R. L. (2009). Propagation of tsunami-driven gravity waves into the thermosphere and ionosphere. *Journal of Geophysical Research*, *114*(A8), A08304. https://doi.org/10.1029/2009JA014105

Hickey, M. P., & Walterscheid, R. L. (2001). Secular variations of OI 5577 Airglow in the mesopause region induced by transient gravity wave packets. *Geophysical Research Letters*, *28*(4), 701–704. https://doi.org/10.1029/2000GL012099

Hocke, K., & Tsuda, T. (2001). Gravity waves and ionospheric irregularities over tropical convection zones observed by GPS/MET radio occultation. *Geophysical Research Letters*, *28*(14), 2815–2818. https://doi.org/10.1029/2001GL013076

Huang, C. S., & Kelley, M. C. (1996). Numerical simulations of gravity wave modulation of midlatitude sporadic E layers. *Journal of Geophysical Research*, *101*(A11), 24533–24543. https://doi.org/10.1029/96JA023327

Jacobi, C., Arras, C., Geißler, C., & Lilienthal, F. (2019). Quarterdiurnal signature in sporadic E occurrence rates and comparison with neutral wind shear. *Annales Geophysicae*, *37*(3), 273–288. https://doi.org/10.5194/angeo-37-273-2019

Jin, H., Miyoshi, Y., Fujiwara, H., & Shinagawa, H. (2008). Electrodynamics of the formation of ionospheric wave number 4 longitudinal structure. *Journal of Geophysical Research*, *113*(A9), A09307. https://doi.org/10.1029/2008JA013301

Kobayashi, S., Ota, Y., Harada, Y., Ebita, A., Moriya, M., Onoda, H., et al. (2015). The JRA-55 Reanalysis: General specifications and basic characteristics. *Journal of the Meteorological Society of Japan. Ser. II*, *93*(1), 5–48. https://doi.org/10.2151/jmsj.2015-001

Larsen, M. F. (2002). Winds and shears in the mesosphere and lower thermosphere: Results from four decades of chemical release wind measurements. *Journal of Geophysical Research*, *107*(A8), SIA 28-1–SIA 28-14. https://doi.org/10.1029/2001JA000218

Liu, H.-L., Bardeen, C. G., Foster, B. T., Lauritzen, P., Liu, J., Lu, G., et al. (2018). Development and validation of the Whole Atmosphere Community Climate Model with Thermosphere and Ionosphere Extension (WACCM-X 2.0). *Journal of Advances in Modeling Earth Systems*, *10*(2), 381–402. https://doi.org/10.1002/2017MS001232

Liu, H., Pedatella, N., & Hocke, K. (2017). Medium-scale gravity wave activity in the bottomside F region in tropical regions. *Geophysical Research Letters*, *44*(14), 7099–7105. https://doi.org/10.1002/2017GL073855

Liu, X., Xu, J., Liu, H.-L., Yue, J., & Yuan, W. (2014). Simulations of large winds and wind shears induced by gravity wave breaking in the mesosphere and lower thermosphere (MLT) region. *Annales Geophysicae*, *32*(5), 543–552. https://doi.org/10.5194/angeo-32-543-2014

Lu, X., Liu, A. Z., Swenson, G. R., Li, T., Leblanc, T., & McDermid, I. S. (2009). Gravity wave propagation and dissipation from the stratosphere to the lower thermosphere. *Journal of Geophysical Research*, *114*(D11), D11101. https://doi.org/10.1029/2008JD010112

Maeda, J., & Heki, K. (2014). Two-dimensional observations of midlatitude sporadic E irregularities with a dense GPS array in Japan. *Earth Planets and Space*, *49*(1), 28–35. https://doi.org/10.1002/2013RS005295

Maeda, J., & Heki, K. (2015). Morphology and dynamics of daytime mid-latitude sporadic E patches revealed by GPS total electron content observations in Japan. *Earth Planets and Space*, *67*(1), 89. https://doi.org/10.1186/s40623-015-0257-4

Miyahara, S., Yoshida, Y., & Miyoshi, Y. (1993). Dynamic coupling between the lower and upper atmosphere by tides and gravity waves. *Journal of Atmospheric and Terrestrial Physics*, *55*(7), 1039–1053. https://doi.org/10.1016/0021-9169(93)90096-H

Miyoshi, Y., & Fujiwara, H. (2003). Day-to-day variations of migrating diurnal tide simulated by a GCM from the ground surface to the exobase. *Geophysical Research Letters*, *30*(15), 1789. https://doi.org/10.1029/2003GL017695

Miyoshi, Y., & Fujiwara, H. (2008). Gravity waves in the thermosphere simulated by a general circulation model. *Journal of Geophysical Research*, *113*(D1), D01101. https://doi.org/10.1029/2007JD008874

Miyoshi, Y., Hitoshi, F., Hidekatsu, J., & Hiroyuki, S. (2014). A global view of gravity waves in the thermosphere simulated by a general circulation model. *Journal of Geophysical Research: Space Physics*, *119*(7), 5807–5820. https://doi.org/10.1002/2014JA019848

Nygren, T., Jalonen, L., Oksman, J., & Turunen, T. (1984). The role of the electric field and neutral wind direction in the formation of sporadic E-layers. *Journal of Atmospheric and Solar-Terrestrial Physics*, *46*(4), 373–381. https://doi.org/10.1016/0021-9169(84)90122-3

Plane, J. M. C., Wuhu, F., & Dawkins, E. C. M. (2015). The mesosphere and metals: Chemistry and changes. *Chemical Reviews*, *115*(10), 4497–4541. https://doi.org/10.1021/cr500501m

Qiu, L. H., Lu, X., Yu, T., Yamazaki, Y., Liu, H. X., Sun, Y. Y., et al. (2023). Horizontal structure of convergent wind shear associated with sporadic E layers over East Asia. *Earth and Planetary Physics*, *7*(5), 1–10. https://doi.org/10.26464/epp2023071

Qiu, L. H., Yu, T., Yan, X. X., Sun, Y. Y., Zuo, X. X., Yang, N., et al. (2021). Altitudinal and latitudinal variations in ionospheric sporadic-E layer obtained from FORMOSAT-3/COSMIC radio occultation. *Journal of Geophysical Research: Space Physics*, *126*(9), e2021JA029454. https://doi.org/10.1029/2021JA029454

Qiu, L. H., Zuo, X., Yu, T., Sun, Y. Y., & Qi, Y. (2019). Comparison of global morphologies of vertical ion convergence and sporadic E occurrence rate. *Advances in Space Research*, *63*(11), 3606–3611. https://doi.org/10.1016/j.asr.2019.02.024

Resende, L. C. A., Batista, I. S., Denardini, C. M., Carrasco, A. J., de Fátima Andrioli, V., Moro, J., et al. (2016). Competition between winds and electric fields in the formation of blanketing sporadic E layers at equatorial regions. *Earth Planets and Space*, *68*(1), 201. https://doi.org/10.1186/s40623-016-05577-z

Sato, K., Yasui, R., & Miyoshi, Y. (2018). The momentum budget in the stratosphere, mesosphere, and lower thermosphere. Part 1: Contributions of different wave types and in situ generation of Rossby waves. *Journal of the Atmospheric Sciences*, *75*(10), 3613–3633. https://doi.org/10.1175/JAS-D-17-0336.1

Shinagawa, H., Miyoshi, Y., Jin, H., & Fujiwara, H. (2017). Global distribution of neutral wind shear associated with sporadic E layers derived from GAIA. *Journal of Geophysical Research: Space Physics*, *122*(4), 4450–4465. https://doi.org/10.1002/2016JA023778

Sobhkhiz-Miandehi, S., Yamazaki, Y., Arras, C., Miyoshi, Y., & Shinagawa, H. (2022). Comparison of the tidal signatures in sporadic E and vertical ion convergence rate, using FORMOSAT-3/COSMIC radio occultation observations and GAIA model. *Earth Planets and Space*, *74*(1), 88. https://doi.org/10.1186/s40623-022-01637-y

Sun, W., Zhao, X., Hu, L., Yang, S., Xie, H., Chang, S., et al. (2021). Morphological characteristics of thousand-kilometer-scale E_s structures over China. *Journal of Geophysical Research: Space Physics*, *126*(2), e2020JA028712. https://doi.org/10.1029/2020JA028712

Tsai, L. C., Shin-Yi, S., Chao-Han, L., Harald, S., Wichert, J., & Mahdi Alizadeh, M. (2018). Global morphology of ionospheric sporadic E layer from the FormoSat-3/COSMIC GPS radio occultation experiment. *GPS Solutions*, *22*(4), 118. https://doi.org/10.1007/s1029-018-0782-2

Tsuda, T., Nishida, M., Rocken, C., & Ware, R. H. (2000). A global morphology of gravity wave activity in the stratosphere revealed by the GPS occultation data (GPS/MET). *Journal of Geophysical Research*, *105*(D6), 7257–7273. https://doi.org/10.1029/GL017i006p00725

Wang, J., Zuo, X., Sun, Y. Y., Yu, T., Wang, Y., Qiu, L. H., et al. (2021). Multilayered sporadic-E response to the annular solar eclipse on June 21, 2020. *Space Weather*, *19*(3), e2020SW002643. https://doi.org/10.1029/2020SW002643

Whitehead, J. D. (1989). Recent work on mid-latitude and equatorial sporadic-E. *Journal of Atmospheric and Solar-Terrestrial Physics*, *51*(5), 401–424. https://doi.org/10.1016/0021-9169(89)90122-0

Whitehead, J. D. (1960). The formation of the sporadic E layer in the temperate zones. *Journal of Atmospheric and Solar-Terrestrial Physics*, *20*(1), 49–58. https://doi.org/10.1016/0021-9169(61)90097-6

Wu, J., Feng, W., Liu, H.-L., Xue, X., Marsh, D. R., & Plane, J. M. C. (2021). Self-consistent global transport of metallic ions with WACCM-X. *Atmospheric Chemistry and Physics*, *21*(20), 15619–15630. https://doi.org/10.5194/acp-21-15619-2021

Yamazaki, Y., Arras, C., Andoh, S., Miyoshi, Y., Shinagawa, H., Harding, B. J., et al. (2021). Examining the wind shear theory of sporadic E with ICON/MIGHTI winds and COSMIC-2 radio occultation Data. *Geophysical Research Letters*, *49*(1), e2021GL096202. https://doi.org/10.1029/2021GL096202

Yamazaki, Y., Harding, B. J., Qiu, L., Stolle, C., Siddiqui, T. A., Miyoshi, Y., et al. (2023). Monthly climatologies of zonal-mean and tidal winds in the thermosphere as observed by ICON/MIGHTI during April 2020–March 2022. *Earth and Space Science*, *10*(6), e2023EA002962. https://doi.org/10.1029/2023EA002962

Yu, B., Xue, X., Yue, X. A., Yang, C., Yu, C., Dou, X., et al. (2019). The global climatology of the intensity of ionospheric sporadic E layer. *Atmospheric Chemistry and Physics*, *19*(6), 4139–4151. https://doi.org/10.5194/acp-2018-790

Yu, T. (2023). Data for Es layer simulations [Dataset]. Zenodo. https://doi.org/10.5281/zenodo.7844587

Yue, X., Schreiner, W., Pedatella, N., & Kuo, Y.-H. (2016). Characterizing GPS radio occultation loss of lock due to ionospheric weather. *Space Weather*, *14*(4), 285–299. https://doi.org/10.1002/2015SW001340

Zeng, Z., & Sokolovskiy, S. (2010). Effect of sporadic E clouds on GPS radio occultation signals. *Geophysical Research Letters*, *37*(18), L18817. https://doi.org/10.1029/2010GL044561

Zuo, X., Wan, W., & Tan, H. (2006). Observational evidences and simulation of tide wind induced mid-latitude sporadic-E layers. *Chinese Journal of Space Science*, *26*(5), 346. https://doi.org/10.11728/cjss2006.05.236